DOI 10.24425/aee.2026.158259

Comparison of electromagnetic exposures from the positioning antenna of driverless vehicle in adult and child passengers

XUWEI DONG ✉, YUFEI REN, MAI LU

Key Laboratory of Opto-Electronic Technology and Intelligent Control of Ministry of Education
Lanzhou Jiaotong University
Gansu Province, China

e-mail: ✉ *dxw007@lzjtu.edu.com, 12232052@stu.lzjtu.edu.com, mai.lu@hotmail.com*

(Received: 26.09.2025, revised: 24.04.2026)

Abstract: With the rapid development of driverless systems technologies, the differences in electromagnetic exposure levels amongst passengers of different ages have become a research hotspot in this field. This study focuses on the electromagnetic exposure of adults and children inside an electric vehicle caused by positioning antennas of driverless systems. Based on the COMSOL Multiphysics software, an electromagnetic numerical calculation model is established, including a vehicle body model, an antenna model, and separate models for an adult and child. Considering the differences in body size and dielectric properties between adults and children, the finite element method is used to calculate exposure levels under the electromagnetic environment generated by the positioning antenna. The results reveal that the electromagnetic exposure level in a child's body is higher than that in an adult due to the former's smaller body size and higher dielectric parameters. This study facilitates the evaluation of the electromagnetic environment of positioning antennas in electric vehicle driverless systems, provides a basis for improving electromagnetic radiation safety standards inside electric vehicles, and promotes the rapid development of electric driverless technologies while ensuring public health and safety.

Key words: adult model, child model, electromagnetic exposure, finite element method, positioning antenna

1. Introduction

With the rapid development of intelligent transportation technologies, electric vehicle driverless systems (EV-DSs) are gradually becoming an important choice for people's future travels [1]. This driverless system mainly relies on high-precision positioning antennas for accurate navigation [2].

However, the radio-frequency electromagnetic fields (RF-EMFs) generated during signal transmission or reception by these positioning antennas may create potential health risks for passengers [3]. The proliferation of driverless systems has resulted in more complex electromagnetic environments inside these vehicles; particularly the electromagnetic environment generated by positioning antennas may have different effects on passengers of different ages.

RF-EMF, as a typical non-ionizing radiation source, is prevalent in various daily scenarios [4], with sources including mobile communication base stations, wireless network devices and household appliances. Notably, the rapid advancements in wireless communication technologies have resulted in a significantly increased frequency and intensity of human exposure to EMF [5]. During the critical period of children's physical development, the tissue water content and dielectric properties of their organs and tissues differ significantly from those of adults. This means that under the same exposure conditions inside EVs, children may face greater exposure levels than adults [6].

The World Health Organization (WHO) [7] and the International Commission on Non-Ionizing Radiation Protection (ICNIRP) [8] recommend strengthening studies on children's electromagnetic exposure levels. In 2002, the International Agency for Research on Cancer (IARC) classified extremely low frequency electromagnetic fields (ELF-EMFs) as a Group 2B possible carcinogen, with related studies primarily focusing on the association between childhood leukemia and ELF-EMF [9]. Divan *et al*. found that long-term exposure to ELF-EMF environments $\geq 0.4\ \mu$T may potentially double the risk of childhood leukemia [10]. However, a multinational collaborative study suggested this conclusion might be influenced by confounding factors in residential environments, thus requiring further verification [11]. Regarding behavioural and neuro developmental aspects, Divan *et al*. found that frequent mobile phone use by mothers during pregnancy might also increase the risk of hyperactivity disorders in their offspring [12]. Kühn *et al*. found through numerical simulations that the absorption rate of RF-EMF by a child's head was 10%–20% higher than that of an adult [13].

The accuracy of EMF exposure assessment partly depends on the dielectric parameters of different tissues, but most existing studies directly adopt dielectric parameters derived from adult tissues. Earlier research by Gabriel *et al*. showed that children, as a special population, have fundamental differences in tissue dielectric properties with adults [14]. In particular, during their growth and development stages, children show significant differences from adults in tissue water content and ion concentration, amongst other parameters. As such, the direct application of adult dielectric parameters may lead to deviations in subsequent exposure assessment results [15].

Vitas *et al*. employed a multilayer concentric spherical head model to compare specific absorption rate (SAR) differences amongst adults and 4-, 8-, 12- and 16-year-old children under 900 MHz dipole radiation. Due to the thinner skull of children, the SAR of the brain decreases as they grow older when exposed to 900 MHz radio frequency. However, the study used identical dielectric parameters for all age groups without considering their differential impacts on human exposure [16]. Wang *et al*. analyzed differences in electromagnetic energy absorption characteristics between adult and child heads from 900 MHz mobile phones. Although they employed region-specific scaling for child head models, they did not differentiate dielectric parameters between adults and children [17]. Zhou *et al*. calculated electromagnetic energy absorption differences between child and adult models at 3 GHz, approximating child tissue dielectric parameters as 10%–40% higher than those of adults [18]. Mohammed *et al*. investigated SAR levels across ages when children or their parents used mobile phones, accounting for age-related dielectric property variations by deriving child parameters from adult tissue dielectric characteristics through numerical relationships [19].

Tognola *et al*. evaluated whole-body SAR effects from 5.9 GHz vehicle-to-vehicle communication RF-EMF in urban environments across age groups; however, they did not consider dielectric property differences between children and adults [20]. Wessapan *et al*. found that 900 MHz mobile phone radiation caused greater electromagnetic energy absorption in children's heads due to their higher permittivity and conductivity, resulting in deeper wave penetration, elevated SAR in the brain and more pronounced temperature rise [21]. Consequently, children's distinct anatomical developmental characteristics and differing biological tissue dielectric properties may lead to higher health risks under identical RF-EMF exposure conditions compared with adults.

This study aims to reveal the differences in electromagnetic exposure between adults and children resulting from radiation generated by the EV-DS positioning antenna. An electromagnetic environment model incorporating an electric vehicle (EV) body, positioning antenna, adult and child passengers is constructed using COMSOL Multiphysics software. The model calculates the induced electric fields (E-fields), SAR and temperature variations generated by 1.575 GHz positioning antenna radiation in both adult and child passengers, while simultaneously analyzing their exposure dose differences. Considering that the research on electromagnetic exposure in the EV-DS scenario still needs to be further improved, evaluating the differences between adults and children in terms of electromagnetic exposure caused by the positioning of the antenna has great significance for improving relevant electromagnetic exposure safety standards and optimizing vehicle designs.

2. Materials and methods

2.1. Numerical calculation methods

Bioelectromagnetics is an interdisciplinary field that combines biophysics and electromagnetics and is based on Maxwell's equations. It reveals the intrinsic mechanism of the interaction between EMF and living organisms [22], thus providing critical support for understanding electromagnetic phenomena in life activities. With the rapid advancements in industrialization and intelligent technologies, electromagnetic radiation levels in external environments have become increasingly complex and variable, drawing significant attention to their potential health impacts. This concern has substantially propelled the development of bioelectromagnetics. The RF module of COMSOL Multiphysics software, which solves Maxwell's equations using the finite element method, has emerged as an effective tool for the numerical computation of bioelectromagnetic fields. The module also offers novel approaches for investigating the coupling mechanisms between EMF and biological systems.

In driverless systems, the positioning antenna is typically mounted on the roof of the EV, from which it emits electromagnetic waves during operation. These waves propagate in space and couple with the human body. The SAR serves as the primary physical parameter for evaluating interactions between EMF and biological tissues [23]. It is defined as the electromagnetic power absorbed per unit mass of biological tissue per unit time (W/kg). SAR is expressed by Eq. (1), while SAR_{10g} represents the averaged value over a 10-gram cubic mass.

$$\mathrm{SAR} = \frac{\sigma}{\rho} |\mathrm{E}|^2 = \frac{\omega \varepsilon_0 \varepsilon_r''}{\rho} |\mathrm{E}|^2 , \tag{1}$$

where: σ represents tissue conductivity (S/m), ρ is tissue density (kg/m^3), E is the E-field intensity within tissues (V/m), and ε_r'' is the imaginary part of relative permittivity (loss factor), characterizing the material's electromagnetic loss properties.

When electromagnetic waves (particularly in the RF and microwave bands) interact with biological tissues, partial energy absorption occurs and is converted into thermal energy, leading to increased tissue temperature. This process is described by Pennes' bioheat equation, as shown in Eq. (2) [24]:

$$\rho C \frac{\partial T}{\partial t} = \nabla \cdot (K \nabla T) + \rho_b C_b \omega_b (T_b - T) + Q_{\text{met}} + Q_{\text{ext}}, \tag{2}$$

where: ρ denotes tissue density (kg/m^3), C represents tissue specific heat capacity (J/[kg ·°C]), T refers to the tissue temperature (°C), K is the thermal conductivity (W/[m ·°C]), ρ_b represents blood density (kg/m^3), C_b indicates blood-specific heat capacity (J/[kg ·°C]), ω_b is blood perfusion rate (1/s), T_b represents blood temperature (°C), Q_{met} is the metabolic heat generation (W/m^3), and Q_{ext} is the external heat source (W/m^3).

2.2. Dielectric parameters of human tissues

In bioelectromagnetics, investigating the interaction between human tissues and EMF must thoroughly account for the frequency-dependent dielectric properties of biological tissues. In 1996, Gabriel *et al*. [25] made significant breakthroughs by establishing an innovative fourth-order Cole–Cole dielectric model based on the classical Cole–Cole model. The newer model introduces four relaxation processes to calculate the dielectric properties of biological tissues in the frequency range from 10 Hz–20 GHz. The model is expressed as shown in Eq. (3):

$$\hat{\varepsilon}_r = \varepsilon_r' - j\varepsilon_r'' = \varepsilon_{r\infty} + \sum_{n=1}^{4} \frac{\Delta\varepsilon_n}{1 + (j\omega\tau_n)^{1-\alpha}} + \frac{\sigma_i}{j\omega\varepsilon_0}, \tag{3}$$

where: ε_0 represents the vacuum permittivity, $\hat{\varepsilon}_r$ is the complex relative permittivity, ε_r'' is the loss factor, $\varepsilon_{r\infty}$ is the optical-frequency relative permittivity, $\Delta\varepsilon_n$ is the relative permittivity increment, ω is the angular frequency, τ_n is the central relaxation time (s), α is the relaxation distribution parameter ($0 \leq \alpha \leq 1$), and σ_i is the ionic conductivity (S/m).

Based on the fourth-order Cole–Cole model, the present study calculates the relative permittivity and conductivity of eight adult tissues at a 1.575 GHz frequency. The dielectric parameters of the torso are determined by averaging values across five tissue types: skin, muscle, fat, blood and bone [26,27]. Research indicates significant physiological differences between developing children and adults: children's tissues exhibit substantially higher water content, while their smaller body dimensions may concentrate electromagnetic energy distribution, resulting in greater biological sensitivity to EMF [28].

Given the absence of experimentally measured dielectric property data for paediatric tissues, mathematical extrapolation from adult data has become a standard methodological approach [29]. For example, Lee *et al*. demonstrated that dielectric parameters for 7-year-old children exceeded adult values by 26%–30% [30]. Consequently, this study adopts dielectric parameters of paediatric tissues that are 30% higher than corresponding adult values. Due to existing limitations in paediatric tissue data, this study maintained identical density, specific heat capacity and thermal conductivity parameters between children and adults [21], all sourced from the 'Tissue Properties Database' published in the Virtual Population models [31]. The tissue parameters of adults and children are shown in Table 1.

Table 1. Human tissue parameters at 1.575 GHz for adults and children

Tissue	Adults		Children		ρ (kg/m^3)	C (J/kg·°C)	k (W/m·°C)
	ε	σ (*S/m*)	ε	σ (*S/m*)			
White matter	37.358	0.824	48.565	1.072	1 041	3 583	0.48
Cerebellum	46.686	1.588	60.692	2.060	1 045	3 653	0.51
Heart	59.964	1.622	77.952	2.109	1 065.4	3 651.5	0.54
Liver	44.695	1.168	58.104	1.519	1 078.75	3 540	0.52
Lung	49.780	1.159	64.714	1.507	394	3 886	0.39
Kidney	55.165	1.799	71.712	2.340	1 066.25	3 763	0.53
Skull	19.649	0.520	25.544	0.676	1 908	1 313	0.32
Trunk	35.588	0.962	46.264	1.251	1 213	2 818	0.38

3. Numerical calculation model

3.1. Antenna model

Supported by the Global Navigation Satellite System (GNSS), EV driverless technologies have achieved groundbreaking milestones in high-precision positioning and navigation, substantially enhancing accuracy and reliability [32]. By receiving real-time signals from the GNSS, the vehicle can accurately obtain its longitude, latitude, altitude and velocity information. Circularly polarized patch antennas have become critical components of GNSS high-precision positioning due to their compact structure, stable performance and excellent anti-interference capabilities [33]. Circularly polarized patch antennas typically adopt microstrip structures, achieving right-hand circular polarization (RHCP) through specialized feeding designs [34]. As shown in Fig. 1, the positioning antenna is designed with a square patch structure using coaxial single-point feeding, operating at the central L1 band (1.575 GHz), with a matched impedance of 50 Ω and an input power of 0.25 W.

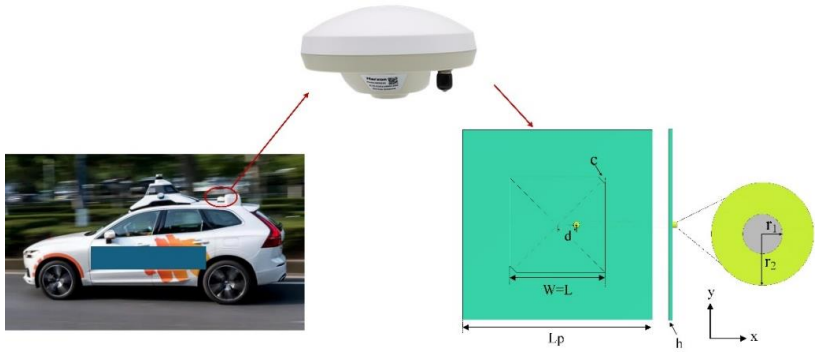

Fig. 1. Positioning antenna structure

An initial square patch is constructed on a 100mm substrate, with the patch side length determined by Eq. (4):

$$W = \frac{c_0}{2f_0\sqrt{\varepsilon_r}} = \frac{\lambda_0}{2\sqrt{\varepsilon_r}}, \tag{4}$$

where: c_0 is the speed of light, λ_0 represents the antenna wavelength, and f_0 is the antenna operating frequency, the substrate's relative permittivity (ε_r) is 3.38. The feed point position governs the antenna's input impedance. In Eq. (5), d is the x-direction feed position when $y = 0$:

$$d = \frac{L}{2}\left(1 - \frac{1}{\varepsilon_e}\right), \tag{5}$$

where ε_e represents the effective dielectric constant, defined by Eq. (6):

$$\varepsilon_e = \frac{\varepsilon_r + 1}{2} + \frac{\varepsilon_r - 1}{2}\left(1 + 12\frac{h}{L}\right)^{-\frac{1}{2}}. \tag{6}$$

Thus, preliminary calculations and frequency-dependent optimization yield a square patch antenna with side dimensions of $L = W = 50.28$ mm and feed point offset $d = 10$ mm from the centre. Circular polarization is achieved by truncating two diagonally opposite corners of the square patch. When the patch area S varies by ΔS, Equations (7)–(9) are used to define the conditions for achieving circular polarization, where Q_0 represents the patch quality factor. The main parameters of the antenna are summarized in Table 2.

$$S = L \times W, \tag{7}$$

$$\Delta S = \Delta S_1 + \Delta S_2 = c^2, \tag{8}$$

$$\left|\frac{\Delta S}{S}\right| = \frac{1}{2Q_0}. \tag{9}$$

Table 2. The main parameters of the antenna

Parameter name	**Parameter**	**Value (mm)**
Substrate width	L_p	100
Substrate thickness	h	1.524
Patch length	L	50.28
Patch width	W	50.28
Chamfer	c	3.5
Inner conductor radius	r_1	0.6
Coaxial cable radius	r_2	1.63
Position	d	10

When modelling in COMSOL Multiphysics, the radiation boundary employs a perfectly matched layer (PML) with thickness set to $\lambda_0/2$ (where $\lambda_0 = c/f_0$). Antenna gain quantitatively characterizes directional radiation efficiency. Figure 2(a) presents the 3D far-field gain pattern of the designed antenna, demonstrating a maximum gain of 6.8 dBi. The *S*11 parameters of the antenna are shown in Fig. 2(b), with the minimum occurring near 1.575 GHz, thereby indicating excellent impedance matching at this frequency.

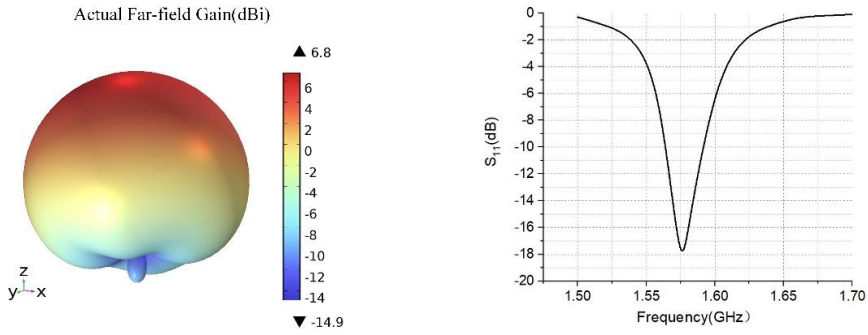

(a) (b)

Fig. 2. Results antenna radiation characteristics: gain pattern (a); *S*11 parameters (b)

3.2. Human body and vehicle models

The human anatomical model that is constructed based on medical images can accurately simulate biological responses, such as electromagnetic radiation and thermal effects, while effectively circumventing ethical concerns and experimental uncertainties associated with in vivo human testing. The adult and child passenger models in this study are selected from the virtual population models, a 34-year-old male (height: 1.77 m, weight: 70.2 kg) and an 11-year-old female (height: 1.49 m, weight: 34.0 kg), respectively [35], as shown in Fig. 3. The human models include major organ tissues: brain white matter, cerebellum, skull, lungs, heart, liver and kidneys.

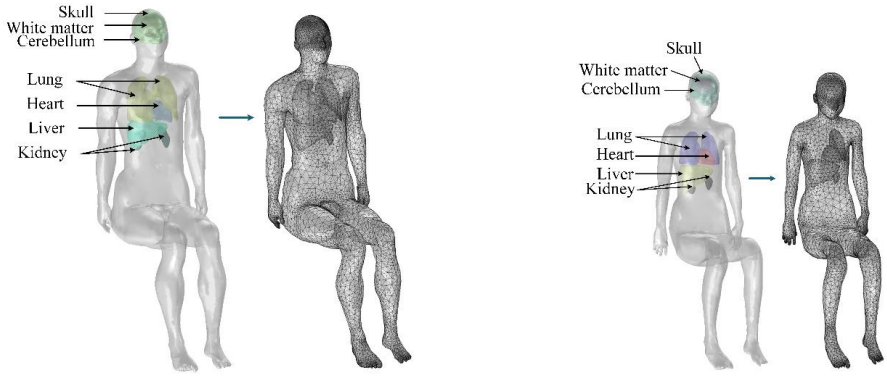

(a) (b)

Fig. 3. Human models: adult human body and finite element model (a);
child human body and finite element model (b)

This study constructs a vehicle body model with 5 207 mm (length) × 2 034 mm (width) × 1 655 mm (height) based on an actual driverless EV, the body is made of aluminium alloy. During the modelling, nonessential components, such as side mirrors and interior trim that do not significantly affect electromagnetic characteristics, are simplified to improve computational efficiency [36]. The vehicle body model, antenna model, and both adult and child human models are imported into COMSOL Multiphysics. The relative spatial positions are shown in Fig. 4.

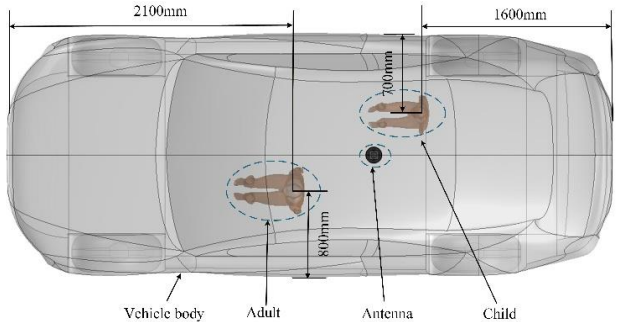

Fig. 4. The relative positioning of human models and radiation source

To ensure calculation accuracy while reducing the need for more computing resources during finite element meshing [37, 38], a denser grid is adopted for complex human body models and antenna models. For the vehicle body, a sparser grid is used. The total number of meshes in the model is approximately 800 000. The mesh grids of the whole model are shown in Fig. 5.

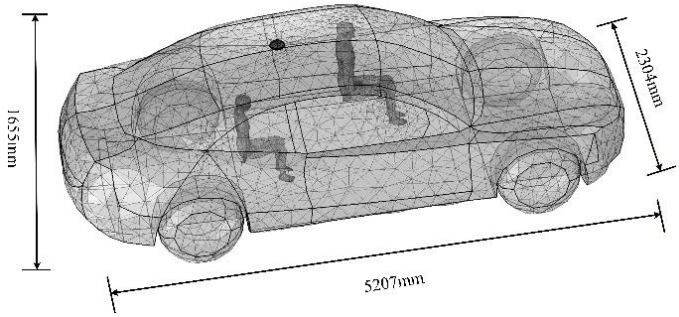

Fig. 5. The mesh grids of the whole model

4. Result

4.1. E-field distribution in the EV body

Figure 6(a) shows the E-field distribution of the EV body when the positioning antenna is operating, while Fig. 6(b) presents different sections of the E-field distribution at varying heights inside the vehicle. As the positioning antenna is located at the rear upper part of the vehicle, the E-field intensity in the rear section of the vehicle body is higher than that in the front section.

Additionally, the E-field strength near the roof area is greater than in regions farther from the roof. The E-field intensity inside the vehicle body is decreased with increasing distance from the antenna. The maximum E-field value generated by the positioning antenna on the vehicle body is 93.3 V/m, with a relatively uniform distribution across the surface, which is consistent with the radiation characteristics of a circularly polarized antenna.

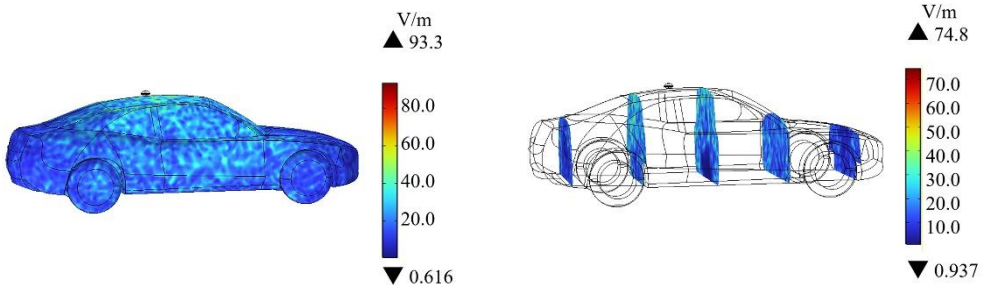

(a) (b)

Fig. 6. E-field distribution in the vehicle body: vehicle body (a); different sections in the vehicle (b)

4.2. Comparison of induced E-field in the adult and child passengers

Figures 7(a) and 7(b) show the induced E-field distributions in the torsos of the adult and child passengers, respectively. The maximum induced E-field is 3.0 V/m for the adult and 23.0 V/m for the child. Compared to the adult, the child shows a higher induced E-field due to the closer proximity to the positioning antenna and higher dielectric parameters. However, the induced E-field distributions in both adult and child torsos remain relatively uniform, consistent with the radiation characteristics of a circularly polarized antenna. Figures 7(c) and 7(d) show the induced E-field distributions in different internal organs of the adult and child passengers, respectively. The maximum values are 0.43 V/m and 4.2 V/m in the adults' and children's organs, respectively. The induced E-field values in the child's organs are significantly higher than those in the adult's. Higher field strengths in the lungs and liver regions for both adults and children are observed, which correlates with the organs' relative positions and dielectric parameters.

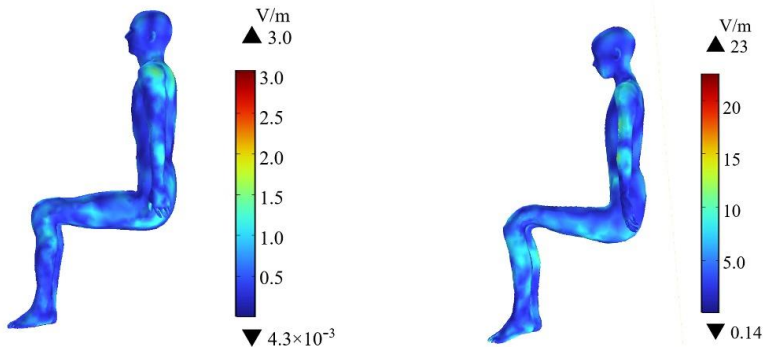

(a) (b)

Figure continued on the next page

Figure continued from the previous page

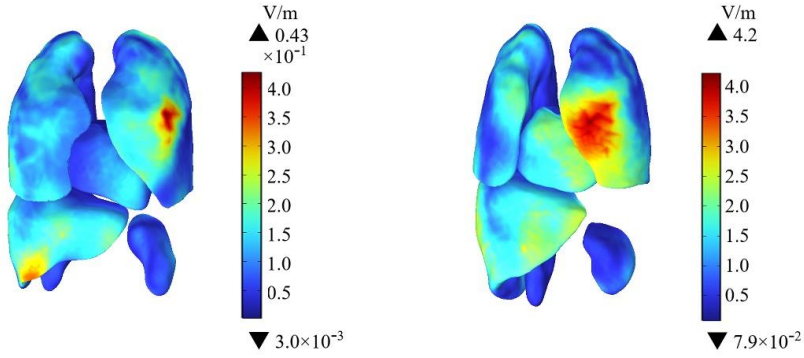

(c) (d)

Fig. 7. The induced E-field distributions in passengers: adult's body (a); child's body (b); different organs of the adult (c); different organs of the child (d)

Compared with the fully mature head of adults, the skull of children is thinner, and the water content of the tissues is higher. There are significant differences in brain development between children and adults, and these differences directly affect electromagnetic wave absorption. Figures 8(a) and 8(b) show the distributions of the induced E-field in the skulls of the adult and child passengers, respectively. The maximum value of the induced E-field in the adult skull is 1.1 V/m, and the areas with relatively large induced E-field values are on both sides of the skull. The maximum value of the induced E-field in the child's skull is 6.6 V/m, and the areas with relatively large induced E-field values are distributed in the front left part of the skull. As the antenna is located on the roof of the vehicle, the values of the induced E-field on the skulls of both adult and child are relatively large. Figures 8(c) and 8(d) show the distributions of the induced E-field in the brain tissues of the adult and child passengers, respectively. Due to the protective effect of the skull on the brain tissues, the induced E-field values are lower than those in the skull. The maximum values of the induced E-field in the brain tissues of the adult and

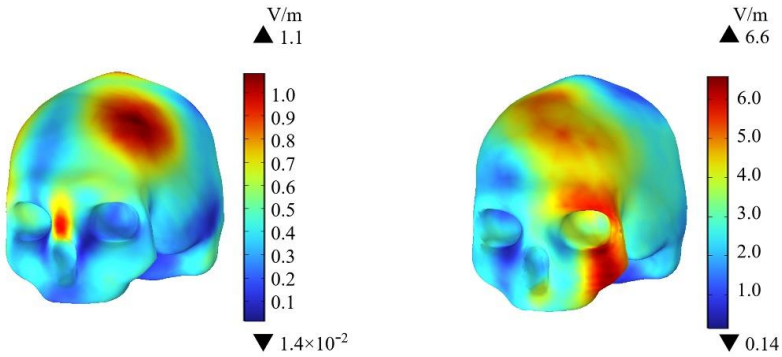

(a) (b)

Figure continued on the next page

Figure continued from the previous page

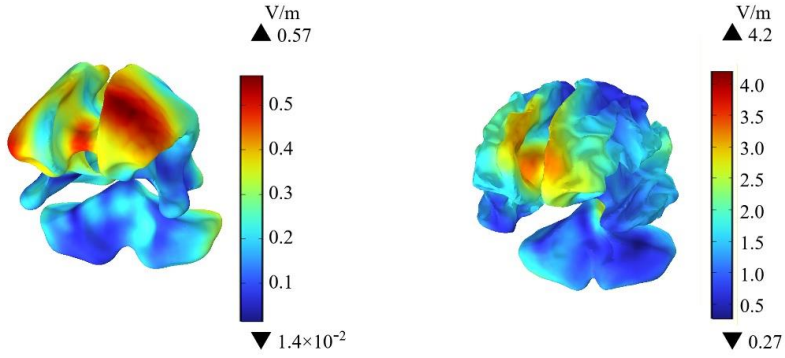

Fig. 8. The induced E-field distributions in the heads: adult's skull (a); child's skull (b); adult's brain tissues (c); child's brain tissues (d)

child passengers are 0.57 and 4.2 V/m, respectively. The value of the induced E-field in the white matter of the brain is higher than that in the cerebellum, which is mainly due to differences in the dielectric parameters and relative positions. The value of the induced E-field in the head of the child passenger is significantly higher than that in the adult passenger.

Figure 9 shows a comparison of the maximum values of the induced E-field in the main organs and tissues of the adult and child passengers. As the child is closer to the exposure source and has larger dielectric parameters, the maximum value of the induced E-field in the child's organs is higher than that in the adult's organs. The induced E-field in the skulls of both is the highest, while the value in the kidney is the lowest, which can be attributed to differences in dielectric parameters and relative positions of various organs.

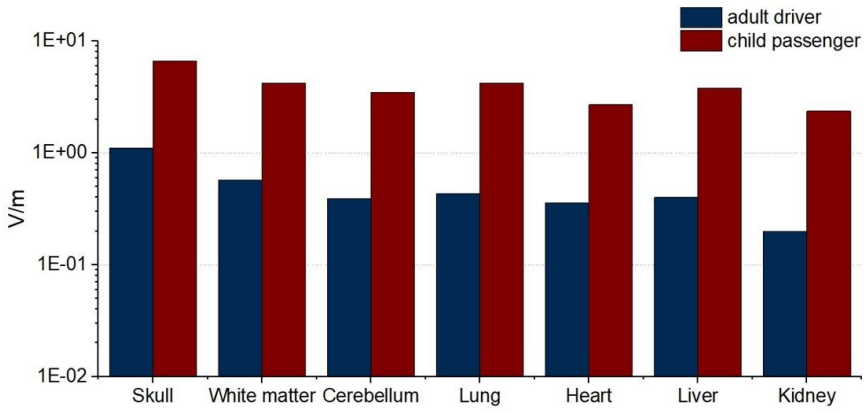

Fig. 9. Comparison of the maximum values of induced E-fields in different tissues of the adult and child passengers

4.3. Comparison of SAR in the adult and child passengers

When the human body absorbs electromagnetic waves, the electromagnetic energy is converted into thermal energy within tissues, which is known as the thermal effect of electromagnetic fields. This thermal effect may interfere with the normal functioning of cells, tissues, and organs. Based on the ICNIRP guidelines, the exposure limits for the general public indicate that the whole-body average SAR must not exceed 0.08 W/kg over a 30-minute exposure period. For localized SAR10g limits, the limbs are subject to a threshold of 4 W/kg, while more stringent standards of 2 W/kg are applied to critical regions, such as the head and torso [8]. In this study, the calculated whole-body average SAR for a child passenger exposed to the electromagnetic field generated by a positioning antenna over 30 minutes is 5.4×10^{-3} W/kg, while that for an adult passenger is 6.5×10^{-5} W/kg. Both average SAR values are well below the exposure limits specified by the ICNIRP guidelines [8].

Figures 10(a) and 10(b) are the SAR_{10g} distributions in the adult and child torsos, respectively. The maximum SAR_{10g} values for the adult and child torsos are 7.3×10^{-4} and 8.4×10^{-2} W/kg, respectively, both remaining below the public exposure limits defined by the ICNIRP guidelines [8].

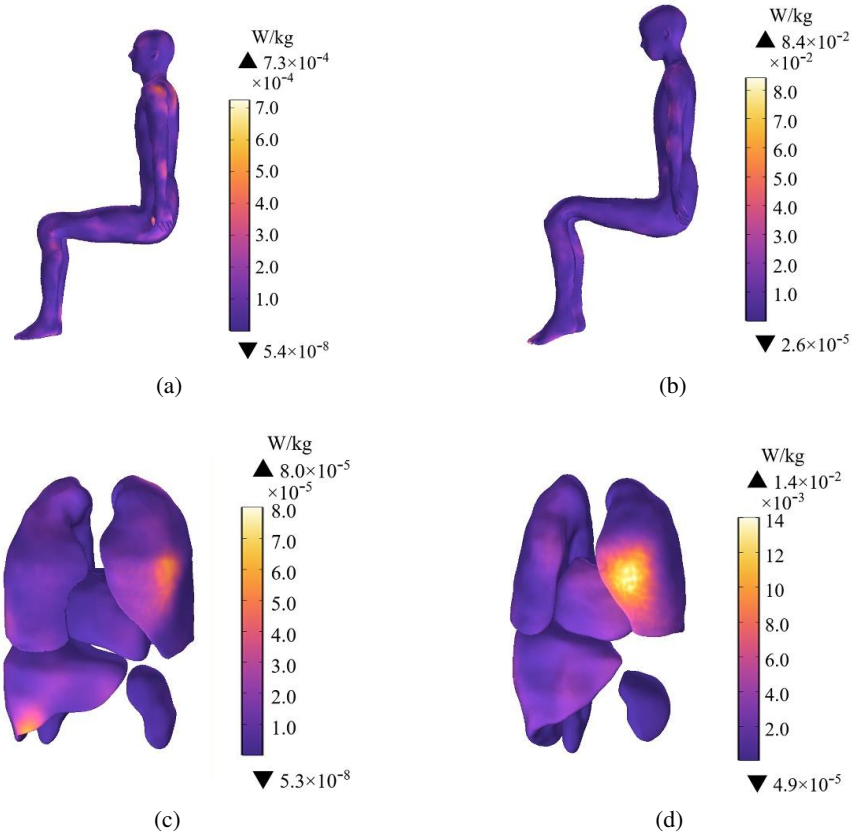

Fig. 10. The SAR_{10g} distributions in passengers: adult's body(a); child's body (b); different organs of the adult (c); different organs of the child (d)

The SAR_{10g} values in both torsos appear relatively uniform, with a higher SAR_{10g} in the child compared to that in the adult. Figures 10(c) and 10(d) present the SAR_{10g} in different internal organs of the adult and child passengers, respectively. The maximum SAR_{10g} values in the different organs of the adult and child passengers are 8.0×10^{-5} and 1.4×10^{-2} W/kg, respectively. As the distance of the child passenger from the antenna is closer and their dielectric parameters are greater than those of the adult, the SAR_{10g} is higher for children. However, the maximum SAR_{10g} in the different organs of adult and child passengers is in both the lung and liver.

Figures 11(a) and 11(b) present the SAR_{10g} in the skulls of the adult and child passengers, respectively. The maximum SAR_{10g} value in the adult's skull is 2.2×10^{-4} W/kg, with the higher SAR_{10g} localized bilaterally in the skull region. In contrast, the maximum SAR_{10g} value in the child's skull is 1.1×10^{-2} W/kg, with the higher SAR_{10g} values concentrated in the frontal skull region. Figures 11(c) and 11(d) present the SAR_{10g} distributions in brain tissues of adult and

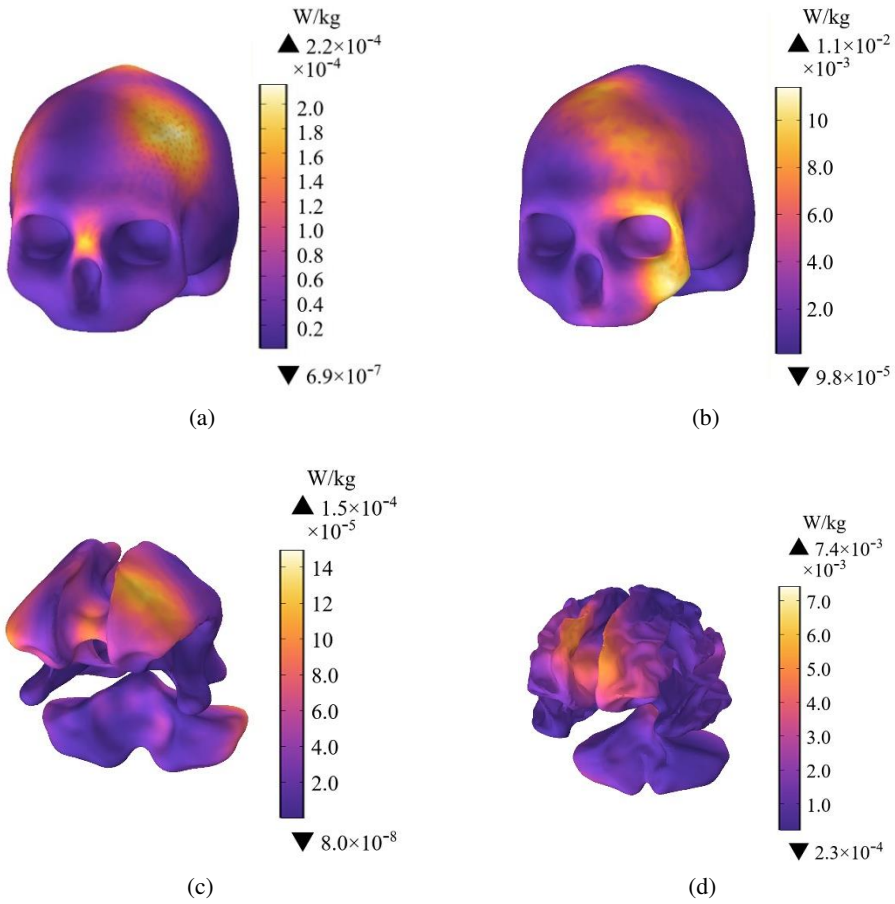

Fig. 11. The SAR_{10g} distributions in the heads: adult's skull (a); child's skull (b); adult's brain tissues (c); child's brain tissues (d)

child passengers, respectively. The maximum SAR_{10g} values in brain tissues in adult and child passengers are 1.5×10^{-4} W/kg and 7.4×10^{-3} W/kg, respectively. Due to the protective effect of the skull, the SAR_{10g} in brain tissue remains lower than that in the skulls of both adults and children. This difference can be attributed to the child's closer proximity to the antenna and higher dielectric parameters, resulting in greater SAR_{10g} values compared to the adult. However, the SAR_{10g} values for both passengers do not exceed the limits defined by the ICNIRP guidelines [8].

Figure 12 shows the maximum SAR_{10g} values in major organs and tissues of the adult and child passengers.

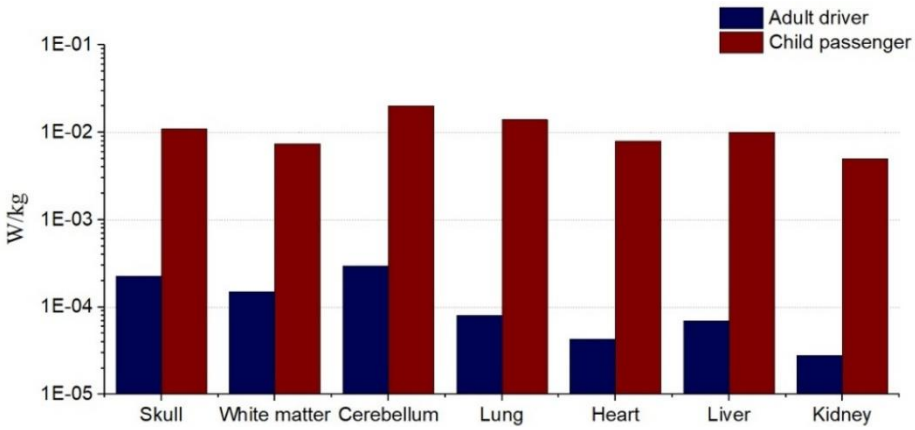

Fig. 12. Comparative of the maximum SAR_{10g} values in different tissues of the adult and child passengers

For different internal organs, the maximum SAR_{10g} values for both are localized in the lung, while the minimum values are in the kidney. These findings can be attributed to the dielectric parameters of the organs and their relative spatial positions. Overall, due to the child's higher dielectric parameters, the SAR_{10g} values in different organs are significantly greater than those in the adult. However, the SAR_{10g} values in major organs and tissues for the adult and child passengers remained below the exposure limits defined by the ICNIRP guidelines [8].

4.4. Comparison of temperature rise in the adult and child passengers

When exposed to RF-EMF, the human body absorbs electromagnetic wave energy, which, when accumulated, may lead to increased body temperature. To ensure that the temperature rise remains within safe limits, the ICNIRP has established a 1.0°C increase in human tissue temperature as the threshold for potential adverse health effects [8]. In this study, the initial body temperature is 36.5°C. Then, the temperature rise under radiation from the positioning antenna is calculated for both adult and child passengers.

Figures 13(a) and 13(b) show the temperature rises in the torsos of the adult and child passengers, respectively. The maximum temperature rises are 0.46°C and 0.47°C for the adult and child passengers, respectively, with a difference of only 0.01°C. Both values are well below the public exposure limit defined by the ICNIRP guidelines [8]. The temperature rise in the torso is relatively uniform in both, with little difference in the degree of temperature rise. Figures 13(c)

and 13(d) show the temperature rises in the different organs of the adult and child passengers, respectively. The maximum temperature rise in the adult organs is 0.56°C, while that in the child's organs is 0.55°C. The maximum temperature rise in the child's organs is 0.01°C lower than that in the adults. Both passengers experienced a significant increase in lung temperature, which is likely due to their significantly lower density compared to other organs.

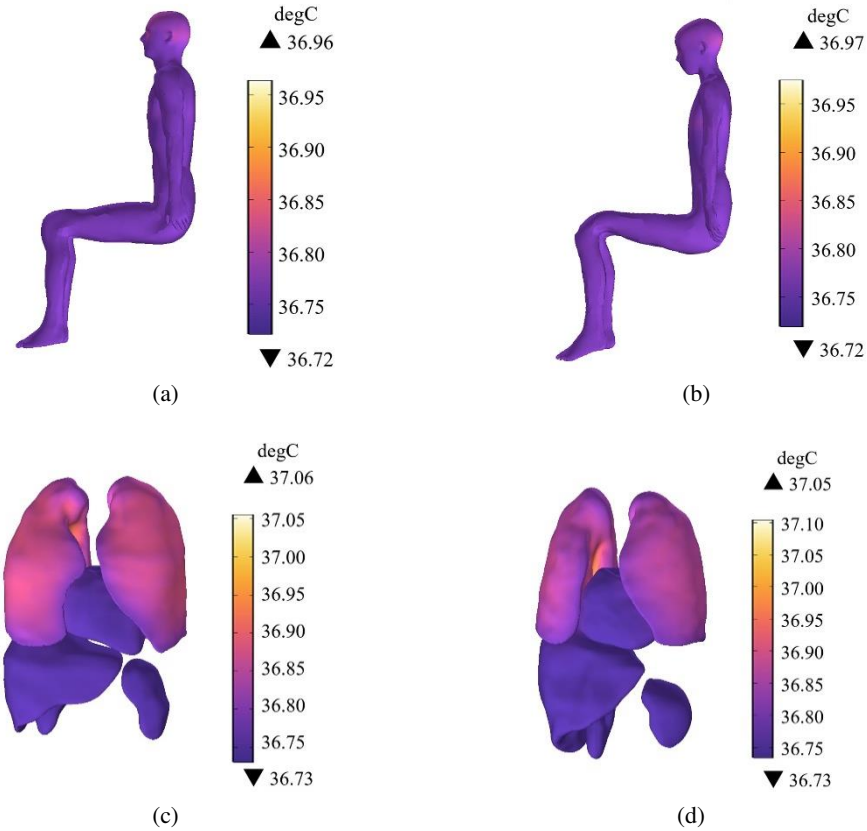

Fig. 13. The temperature rises in passengers: adult's body (a); child's body (b); different organs of the adult (c); different organs of the child (d)

Figures 14(a) and 14(b) show the temperature rises in the skulls of the adult and child passengers, respectively. The maximum temperature rises in the skulls of the adult and child passengers are 0.39°C and 0.38°C, respectively, with a difference of only 0.01°C. Both values are well below the public exposure limit defined in the ICNIRP guidelines [8]. Figures 14(c) and 14(d) show the temperature rises in the brain tissues of the adult and child passengers, respectively. The maximum temperature rises in the brain tissues of the adult and child passengers are almost 0.26°C. Due to the protective effect of the skull, the temperature rise in the skull is greater than that in the brain tissues.

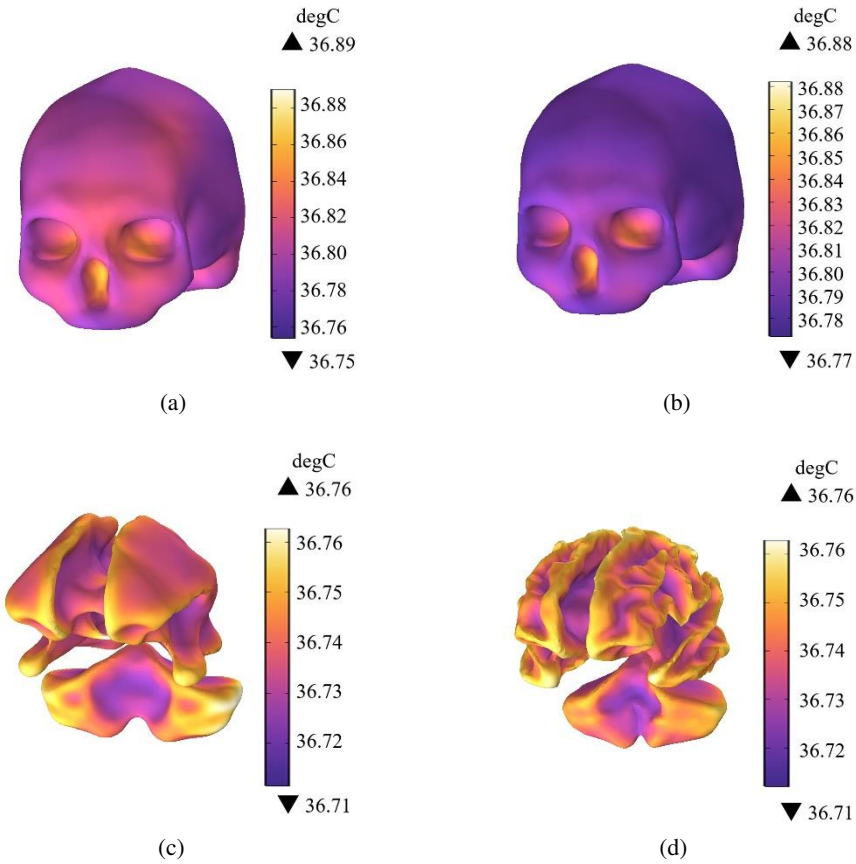

Fig. 14. The temperature rises in the heads: adult's skull (a); child's skull (b); adult's brain tissues (c); child's brain tissues (d)

Additionally, to further compare the temperature rises in different organs and tissues under the radiation of a 1.575 GHz positioning antenna, the temperature rises in different organs and tissues of the adult and child passengers over 90-minutes are calculated. Figure 15(a) shows the temperature rises in different tissues of the adult. In the head, the temperature rise in the skull gradually increased over 90 minutes, reaching a maximum of 37.04°C. The cerebellum and white matter show a rapid temperature rise within the first 0–10 minutes, after which the rate of increase slows down. The trends are almost similar, and after 90 minutes, the temperature rises in the white and grey matter are the smallest. The temperature rise in the lungs is significantly higher than that in other organs and tissues, with a maximum increase of 0.72°C. The temperature rise in other organs is relatively gentle within 90 minutes, with the temperature increase ranging from 0.3°C to 0.5°C. Figure 15(b) presents the temperature rises in different organs of the child passenger. The temperature rises in the child's organs and tissues are similar to those in the adult, with the maximum temperature rise in the organs close to that in the adult. In the head, the skull's temperature rise reached a maximum of 37.02°C. The temperature increase in the

lungs is the greatest amongst all organs, with the maximum temperature increase of 0.68°C, while the temperature increases in other organs range from 0.3°C to 0.5°C. Overall, the temperature rise is faster in the initial stage of radiation exposure and then gradually stabilizes. However, the temperature increases in different tissues and organs of the adult and child passengers do not exceed the 1.0°C limit defined by the ICNIRP [8].

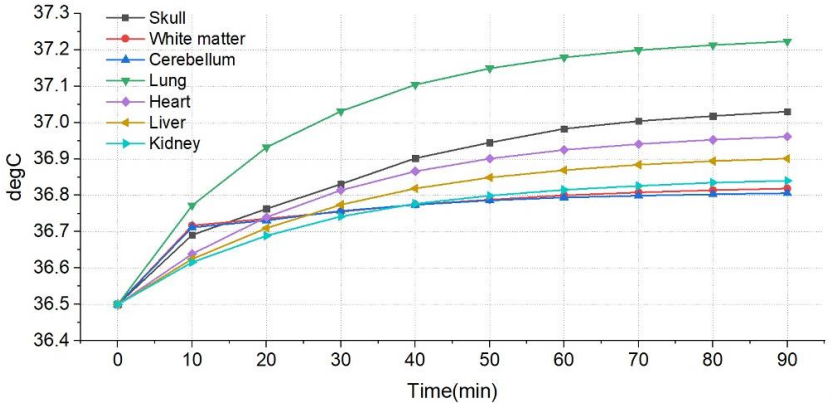

(a)

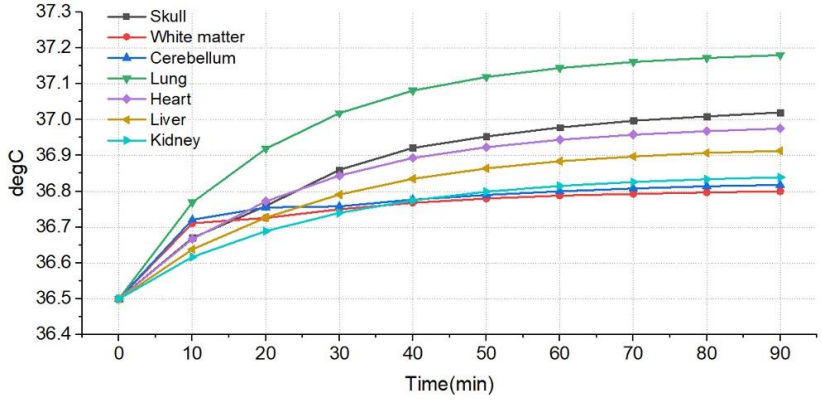

(b)

Fig. 15. Comparison of temperature rises in different organs and tissues over 90-minute: different organs and tissues of the adult (a); different organs and tissues of the child (b)

5. Conclusion

With the rapid development of EV-DS technologies, the potential impact of electromagnetic radiation from positioning antennas, as a key component of driverless systems, has attracted widespread attention. Due to differences in the physiological structure and the dielectric properties

of tissues, adults and children show varying responses to electromagnetic radiation exposure. This study aims to investigate the electromagnetic exposure levels of positioning antennas in EV-DSs for adult and child passengers and analyze their potential health impacts.

The calculation results reveal that the maximum E-field generated by the 1.575 GHz positioning antenna in the EV body is 93.3 V/m. As the distance from the positioning antenna increases, the induced E-field gradually decreases. The maximum induced E-field in the child's body is 23 V/m, which is approximately 8 times higher than that in the adult's body (3.0 V/m). The maximum induced E-field in the child's head (6.6 V/m) is also higher than that in the adult, approximately 6 times the adult's maximum induced E-field (1.1 V/m). Due to the protective effect of the skull, the induced E-field in the brain tissue is relatively lower. Amongst the different organs of the body, the induced E-field in the lungs is the highest, while that in the liver is slightly lower than that of the lungs. The lowest induced E-field is in the kidneys.

The distribution of the SAR_{10g} shows a similar trend, with the maximum SAR_{10g} in a child's body (8.4×10^{-2} W/kg) being approximately 100 times higher than that in an adult's body (7.3×10^{-4} W/kg). Furthermore, the maximum SAR_{10g} in a child's head (1.1×10^{-2} W/kg) is about 50 times greater than that in an adult's head (2.2×10^{-4} W/kg). Amongst all the organs, the SAR_{10g} in the lungs is the largest, followed by the skull; the minimum SAR_{10g} is in the kidneys. The whole-body average SAR values are 5.4×10^{-3} W/kg for child passengers and 6.5×10^{-5} W/kg for adult passengers, respectively. The SAR values for both passengers do not exceed the limits defined by the ICNIRP guidelines. After 30 minutes radiation of the position antenna, the maximum body temperature increases are 0.55°C and 0.56°C in the child and adult passengers, respectively. The highest temperature rise is in the lungs. Furthermore, the temperature increases in different organs are similar, with relatively small differences. All increases are below the 1.0°C limit defined by the ICNIRP.

The results indicate that there are distinct differences in exposure levels for passengers of different ages and positions when exposed to radiation from the EVs' positioning antenna. The induced E-field and SAR in children's bodies are higher than those in adults. This discrepancy arises primarily from the combined effects of body size and tissue dielectric parameters rather than a single factor. In particular, the higher tissue water content in children raises the dielectric parameters of their tissues, which enhances electromagnetic absorption, leading to higher exposure levels under the same exposure scenario. Furthermore, for the same passenger, the electromagnetic exposure levels of different tissues also vary due to differences in dielectric parameters and spatial positions.

Therefore, to ensure the safety of passengers, especially child passengers who are more sensitive to electromagnetic radiation, the issue of electromagnetic exposure for occupants should be especially considered during the design and deployment of driverless systems. By adopting the effective protective method, the potential impacts of electromagnetic radiation from positioning antennas on passengers can also be minimized. The findings of this study not only supplement current research on the electromagnetic environment in driverless vehicles but also provide a reference point for the public to understand the electromagnetic environments of EVs.

Acknowledgements

The study supported by the National Natural Science Foundation of China (52467026), the Natural Science Foundation of Gansu Province (23JRRA889), the Innovation Fund Project of Colleges and Universities in Gansu Province (2024B-057, 2025A-051).

References

[1] Zhu W., Wei J., *Influence of information strategies on behavioral intention to adopt driverless vehicles: Based on a survey experiment*, Energy, vol. 318, 134842 (2025), DOI: 10.1016/j.energy.2025.134842.

[2] Volakis J.L., O'Brien A.J., Chen C.C., *Small and adaptive antennas and arrays for GNSS applications*, Proceedings of the IEEE, vol. 104, no. 6, pp. 1221–1232 (2016), DOI: 10.1109/JPROC.2016.2528165.

[3] Bonato M., Tobnola G., Benini M., Gallucci S., Chiaramello E., Fiocchi S., Parazzini M., *Assessment of SAR in Road-Users from 5G-V2X Vehicular Connectivity Based on Computational Simulations*, Sensors, vol. 22, no. 17, 6564(2022), DOI: 10.3390/s22176564.

[4] Wessapan T., Srisawatdhisukul S., Rattanadecho P., *Specific absorption rate and temperature distributions in human head subjected to mobile phone radiation at different frequencies*, International Journal of Heat and Mass Transfer, vol. 55, no. 1–3, pp. 347–359 (2012), DOI: 10.1016/j.ijheatmasstransfer.2011.09.027.

[5] Sagar S., Dongus S., Schoeni A., *Radiofrequency electromagnetic field exposure in everyday microenvironments in Europe: A systematic literature review*, Journal of Exposure Science and Environmental Epidemiology, vol. 28, no. 2, pp. 147–160 (2018), DOI: 10.1038/jes.2017.13.

[6] Lu M., Ueno S., *Comparison of specific absorption rate induced in brain tissues of a child and an adult using mobile phone*, Journal of Applied Physics, vol. 111, no. 7, 07B311 (2012), DOI: 10.1063/1.3672854.

[7] World Health Organization, *WHO research agenda for radiofrequency fields*, Geneva, Switzerland, World Health Organization (2010).

[8] ICNIRP, *Guidelines for limiting exposure to electromagnetic fields (100 kHz to 300 GHz)*, Health Physics, vol. 118, no. 5, pp. 483–524 (2020), DOI: 10.1097/HP.0000000000001210.

[9] IARC, *Non-ionizing radiation, Part 1: Static and extremely low-frequency (ELF) electric and magnetic fields*, IARC Monographs on the Evaluation of Carcinogenic Risks to Humans, vol. 80, Lyon, France, IARC Press (2002).

[10] Divan H.A., Kheifets L., Obel C., Olsen J., *Prenatal and postnatal exposure to cell phone use and behavioral problems in children*, epidemiology, vol. 19, no. 4, pp. 523–529 (2008), DOI: 10.1097/EDE.0b013e318175dd47.

[11] Cardis E., Armstrong B.K., Bowman J.D. *et al.*, *Risk of brain tumours in relation to estimated RF dose from mobile phones: results from five Interphone countries*, Occupational and Environmental Medicine, vol. 68, no. 9, pp. 631–640 (2011), DOI: 10.1136/oemed-2011-100155.

[12] Divan H.A., Kheifets L., Obel L., Olsen J., *Cell phone use and behavioural problems in young children*, Journal of Epidemiology and Community Health, vol. 66, no. 6, pp. 524–529 (2012), DOI: 10.1136/jech.2010.115402.

[13] Kühn S., Jennings W., Christ A., Kuster N., *Assessment of induced radio-frequency electromagnetic fields in various anatomical human body models*, Physics in Medicine and Biology, vol. 54, no. 4, pp. 875–890 (2009), DOI: 10.1088/0031-9155/54/4/004.

[14] Gabriel C., Gabriel S., Corthout E., *The dielectric properties of biological tissues: I. Literature survey*, Physics in Medicine and Biology, vol. 41, no. 11, pp. 2231–2249 (1996), DOI: 10.1088/0031-9155/41/11/001.

[15] Peyman A., *Dielectric properties of tissues; variation with age and their relevance in exposure of children to electromagnetic fields; state of knowledge*, Progress in Biophysics and Molecular Biology, vol. 107, no. 3, pp. 434–438 (2011), DOI: 10.1016/j.pbiomolbio.2011.08.007.

[16] Anderson V., *Comparisons of peak SAR levels in concentric sphere head models of children and adults for irradiation by a dipole at 900 MHz*, Physics in Medicine and Biology, vol. 48, no. 20, pp. 3263–3275 (2003), DOI: 10.1088/0031-9155/48/20/001.

[17] Wang J., Fujiwara O., *Comparison and evaluation of electromagnetic absorption characteristics in realistic human head models of adult and children for 900-MHz mobile telephones*, IEEE Transactions on Microwave Theory and Techniques, vol. 51, no. 3, pp. 966–971 (2003), DOI: 10.1109/TMTT.2003.808681.

[18] Zhou H.M., Su Z.T., Hu X.J., Xie X.D., Xu D.C., Yang G.S., *A comparative study of electromagnetic energy absorption in children and adults under microwave exposure*, Radiation Protection, vol. 5, no. 29, pp. 311–316 (2009).

[19] Mohammed B., Jin J., Abbosh A.M., Bialkowski S., Manoufali M., Crozier S., *Evaluation of children's exposure to electromagnetic fields of mobile phones using age-specific head models with age-dependent dielectric properties*, IEEE Access, vol. 5, pp. 27345–27353 (2017), DOI: 10.1109/ACCESS.2017.2767074.

[20] Tognola G., Benini M., Bonato M., Gallucci S., Parazzini M., *Assessment of the variability of human exposure to radiofrequency electromagnetic fields arising from 5.9 GHz vehicular communication in urban environments*, Sensors, vol. 23, no. 15, 6802 (2023), DOI: 10.3390/s23156802.

[21] Wessapan T., Rattanadecho P., *Numerical analysis of specific absorption rate and heat transfer in human head subjected to mobile phone radiation: Effects of user age and radiated power*, Journal of Heat Transfer, vol. 134, no. 12, 121101 (2012), DOI: 10.1115/1.4006595.

[22] Reggia J.A., *Generalizing Maxwell's equations to complex-valued electromagnetic fields*, Physica Scripta, vol. 99, no. 1, 015513 (2024), DOI: 10.1088/1402-4896/ad10dc.

[23] Schiavoni A., Bertotto P., Richiardi G., Bielli P., *SAR generated by commercial cellular phones-phone modeling, head modeling, and measurements*, IEEE Transactions on Microwave Theory and Techniques, vol. 48, no. 11, pp. 2064–2071 (2000), DOI: 10.1109/22.884196.

[24] Thurai M., Goodridge V.D., Sheppard R.J., Grant E.H., *Variation with age of the dielectric properties of mouse brain cerebrum*, Physics in Medicine and Biology, vol. 29, no. 9, pp. 1133–1136 (1984), DOI: 10.1088/0031-9155/29/9/009.

[25] Gabriel S., Lau R., Gabriel C., *The dielectric properties of biological tissues: III. Parametric models for the dielectric spectrum of tissues*, Physics in Medicine and Biology, vol. 41, no. 11, pp. 2271–2293 (1996), DOI: 10.1088/0031-9155/41/11/003.

[26] Tian R., Zhang J., Lu M., *Research on the influence of power frequency electric field of pantograph on passengers' health in high-speed EMU*, Archives of Electrical Engineering, vol. 72, no. 2, pp. 483–501 (2023), DOI: 10.24425/aee.2023.145421.

[27] Yang C.Q., Lu M., *Safety evaluation for a high signal operator with electric field exposure induced by contact wires*, Archives of Electrical Engineering, vol. 70, no. 2, pp. 431–444 (2021), DOI: 10.24425/aee.2021.136994.

[28] Peyman A., Rezazadeh A.A., Gabriel C., *Changes in the dielectric properties of rat tissue as a function of age at microwave frequencies*, Physics in Medicine and Biology, vol. 46, no. 12, pp. 1617–1629 (2001), DOI: 10.1088/0031-9155/46/6/303.

[29] Peyman A., Gabriel C., *Cole–Cole parameters for the dielectric properties of porcine tissues as a function of age at microwave frequencies*, Physics in Medicine and Biology, vol. 55, no. 15, pp. N413–N419 (2010), DOI: 10.1088/0031-9155/55/15/N02.

[30] Lee A.K., Choi H.D., Choi J.I., *Study on SARs in head models with different shapes by age using SAM model for mobile phone exposure at 835 MHz*, IEEE Transactions on Electromagnetic Compatibility, vol. 49, no. 2, pp. 302–312 (2007), DOI: 10.1109/TEMC.2007.897124.

[31] Hasgall P.A., Gennaro F.D., Baumgartner C., *IT'IS Database for thermal and electromagnetic parameters of biological tissues*, Version 3.0 (2015), DOI: 10.13099/VIP21000-03-0.

[32] An X., Zhao S., Cui X., Shi Q., Lu M., *Distributed Multi-Antenna Positioning for Automatic-Guided Vehicle*, Sensors, vol. 20, no. 4, 1155 (2020), DOI: 10.3390/s20041155.

[33] Hao S.S., Chen Q.Q., Li J.Y., Xie J., *A High-Gain Circularly Polarized Slotted Patch Antenna*, IEEE Antennas and Wireless Propagation Letters, vol. 19, no. 6, pp. 1022–1026 (2020), DOI: 10.1109/LAWP.2020.2987330.

[34] Lin C.L., Nie Z.P., *Antenna engineering manual*, Publishing House of Electronics Industry (2002).

[35] Gosselin M.C., Neufeld E., Moser H., Huber E., Farcito S., Gerber L., Jedensjo M., Hilber I., Gennaro F.D., Lloyd B., Cherubini E., Szczerba D., Kainz W., Kuster N., *Development of a new generation of high-resolution anatomical models for medical device evaluation: the Virtual Population 3.0*, Physics in Medicine and Biology, vol. 59, no. 18, pp. 5287–5303 (2014), DOI: 10.1088/0031-9155/59/18/5287.

[36] Santis V.D., Giaccone L., Freschi F., *Chassis Influence on the Exposure Assessment of a Compact EV during WPT Recharging Operations*, Magnetochemistry, vol. 7, no. 2, 25 (2021), DOI: 10.3390/magnetochemistry7020025.

[37] Gubernati A.C., Freschi F., Giaccone L., Scorretti R., *Analysis of Numerical Artifacts Using Tetrahedral Meshes in Low Frequency Numerical Dosimetry*, Applied Sciences, vol. 12, no. 13, 6526 (2022), DOI: 10.3390/app12136526.

[38] Kim H.Y., Kim H.G., *A hexahedral-dominant FE meshing technique using trimmed hexahedral elements preserving sharp edges and corners*, Engineering with Computers, vol. 38, no. 5, pp. 4307–4322 (2022), DOI: 10.1007/s00366-021-01526-0.